The Journal of Supercritical Fluids 136 (2018) 95–101

Contents lists available at ScienceDirect

The Journal of Supercritical Fluids

journal homepage: www.elsevier.com/locate/supflu

Dynamic pH determination at high pressure of aqueous additive mixtures in contact with dense CO_2

Martin Andersson[a,*], Irene Rodriguez-Meizoso[b], Charlotta Turner[b], Klas Hjort[a], Lena Klintberg[a]

[a] Uppsala University, Centre of Natural Hazards and Disaster Science, CNDS, Department of Engineering Sciences, Division of Microsystem Technology, Box 534, SE-75121 Uppsala, Sweden

[b] Lund University, Department of Chemistry, Centre for Analysis and Synthesis, P.O. Box 124, SE-22100, Lund, Sweden

GRAPHICAL ABSTRACT

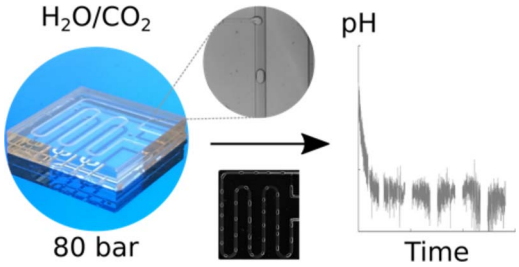

ARTICLE INFO

Keywords:
Supercritical fluid chromatography
High-pressure microfluidics
Additive salts
Dense CO_2
Multiphase flow
Image analysis

ABSTRACT

A system consisting of a high-pressure tolerant microfluidic glass chip, high-speed absorbance imaging, and image processing has been developed to study rapid dynamic events like pH change in a multiphase flow. The system gives both kinetic and quantitative equilibrated information. By tracking the interactions of aqueous additive mixtures and liquid CO_2, at 80 bar and 24 °C, under flow, measurement at a given P, T condition is done in 0.25 s. The acidification rate to steady state was found to be mass transport limited, occurring in less than 1 s. For 30 mM of the additives ammonium acetate and ammonium formate, equilibrium pH of 4.5 and 4.1, respectively, was seen. These additives are of key importance in common mobile phases used in SFC.

1. Introduction

High-pressure microfluidic systems have similar potential in flow-through chemical systems as what their low-pressure counterparts already have shown, *e.g.* by providing isothermal systems with less use of analytes, shorter time constants and, lower dead volumes [1]. For high-pressure applications, microfluidics allows for shorter measuring times and faster evaluations than setups using mL-sized batch cells, as exemplified in phase equilibria studies [2]. While batch cell techniques offer high accuracy, the methods are static and are not able to reveal local, space and time-dependent effects. With the emergence of high-pressure microfluidics, a new tool for dynamically studying these questions is available.

Of high relevance for high-pressure microfluidics and the miniaturization of chromatographic systems is ultra-fast supercritical fluid chromatography (SFC) analysis [3]. Retention times are typically less than 1 min and there is a need to reach mobile phase stability at injection fast. Methods making it possible to study both stability and the dynamics involved when conditions change are important. The highly complex attributes of the mobile phases used in SFC makes these type of measurements challenging.

Chromatographic systems encounter a wide range of flow velocities,

* Corresponding author.
E-mail address: martin.andersson@angstrom.uu.se (M. Andersson).

https://doi.org/10.1016/j.supflu.2018.02.012
Received 21 December 2017; Received in revised form 13 February 2018; Accepted 14 February 2018
Available online 19 February 2018

from 1 to 20 mm/s in columns to several hundred mm/s in tubing, affecting the timescales needed to reach equilibrium conditions. Also, there is a growing trend for the miniaturization of chromatographic systems [4], and as these systems decrease in size, residence times decrease. Meanwhile, SFC is becoming an increasingly competitive method for high-throughput and high-resolution separation of chiral and achiral organic compounds [3,5]. For high-throughput separations, SFC has an advantage as the high diffusivity and low viscosity of supercritical carbon dioxide ($scCO_2$) as the mobile phase allows for a higher efficiency at higher flow rates than for conventional liquid chromatography [3]. However, SFC using CO_2 shows difficulties with separations of highly polar compounds, and for this reason, modifications of the mobile phase by the addition of polar cosolvents and up to approximately 9% water [6], are made [7,8]. Using a similar approach to separate highly polar analytes with increased resolution, enhanced fluidity hydrophilic interaction liquid chromatography uses CO_2, methanol and water [9,10]. Dense CO_2 (less than 20 mol%) in water-methanol mixtures has been used to improve the separation of polar ionizable compounds like nucleosides [11]. In conventional liquid chromatography, the importance between pH and chromatographic performance is well established where, depending on the nature of the analyte, mobile phase composition and, stationary phase, the pH can affect retention factors, peak shape and resolution [12]. For ionizable analytes, changes in the retention factors by more than one order of magnitude over the pH scale are seen when the ionization of the analytes changes [13]. For the now common ternary component mobile phase composed of CO_2, methanol and, water, such effects are considerably more difficult to study [14,15]. As dense CO_2 and water containing cosolvents mix, carbonic acid is formed and dissociated which acidifies the resultant solution [6,16,17]. As this acidification process is connected to the amount of CO_2 present, the pressure drop over the column and variations in pressure and temperature result in dynamic conditions [18]. Further, pH is most often described for aqueous solutions. When non-aqueous components are present, both solvation energies and activity coefficients of the involved species are different [19]. This affects dissociation constants and the interpretation of pH in SFC mobile phases.

While these are aspects to be further studied, the effects on chromatographic performance that mM additions of ammonium salts of simple carboxylic acids have has been investigated by several researchers [20,21], showing how performance parameters, *e.g.* peak shape, can be improved. For SFC mobile phases with a high degree of polarity, dissociation of ionic species becomes a factor in the separation of analytes. When water is added to the mobile phase, protonation and deprotonation of ionizable compounds become increasingly possible as the ion solubility increases. Since CO_2 both have a solubility in water, that varies with temperature and pressure, and can form the ionizable species carbonic acid and bicarbonate, the situation is complex. Both mixing and hydration of CO_2 in aqueous phases takes time and should result in regions with different, local, pH when conditions change. Control of pH conditions is also essential in several other fields, *e.g.* in enzymatic processing [22] and extraction [23], where flowing compressed CO_2-water systems are used. The relevance of pH in water-CO_2 microemulsions is also noted, with extensive studies of additive salts having been made [24,25].

In this paper, a system has been developed consisting of a high-pressure chip for segmented flows in combination with a high-speed camera to study rapid dynamic events. To demonstrate its capabilities, the local and time-dependent variations of pH when an aqueous phase meets with dense CO_2 is explored. By utilizing the immiscibility between CO_2 and water, the aqueous phase can together with an indicator be used to probe the pH effects that dense CO_2 have. Due to the large interest in ammonium acetate ($NH_4CH_3CO_2$) and ammonium formate (NH_4HCO_2) in SFC, these additive salts are further added to the aqueous phase, exploring their effect on changing the pH. By this, a fast method for pH determination for high-pressure applications is demonstrated. With the method having the ability to measure in both time and space, insight into the development of equilibrium in flow systems is generated. While not a direct measurement of the pH in a SFC mobile phase, we show how these salts are affected in a similar, but simpler, environment.

2. Materials and methods

2.1. Materials

The pH indicator BPB (sodium bromophenol blue, Abcam), having two absorption peaks at 436 and 591 nm corresponding to the protonated and deprotonated species, was used at a concentration of 2 mM in all sample and calibration solutions. The sample solutions were made from $NH_4CH_3CO_2$ (ammonium acetate, EMSURE®, Merck) and NH_4HCO_2 (ammonium formate, Acros Organics) at concentrations of either 2, 5, 7, 10, 20 and 30 mM; and 2, 7, 10, 20 and 30 mM, respectively. All solutions were made by weighing the corresponding amount of salt and preparing stock solutions, which then were used to prepare the sample and calibration solutions. Deionised water was used both for preparing the solutions and to record blank images of the channels in the chip. Seven calibration solutions were prepared from citric buffer salts (citric acid monohydrate, Acros Organics, and anhydrous trisodium citrate, Alfa Aesar) covering the pH range 3.0–5.2. For an early version of the setup, used to study the local dynamics at the initial contact point of the fluids, a 7.5 pH test solution containing BPB, NaOH and NaCl was used.

2.2. Experimental setup

The fluid system, Fig. 1, consisted of two separate subsystems to provide the chip with both aqueous solutions and dense CO_2. Each subsystem had a high-pressure piston pump (ISCO DM100, Teledyne) and a 1/16” stainless steel tubing line equipped with check valves and needle valves (41AF1, 11AF1 and 15AF1, High Pressure Equipment Company). Both the pump and fluid line for the CO_2 was kept at 3.5 °C using a water bath, two recirculating heaters (E100, Lauda) and a compressor chiller (RK20, Lauda), keeping the CO_2 liquid in the pump. For the aqueous solution subsystem, a 5 mL sample loop was used to inject sample solutions into the chip, using deionized water both as a pushing medium and to rinse the system between samples. Just before

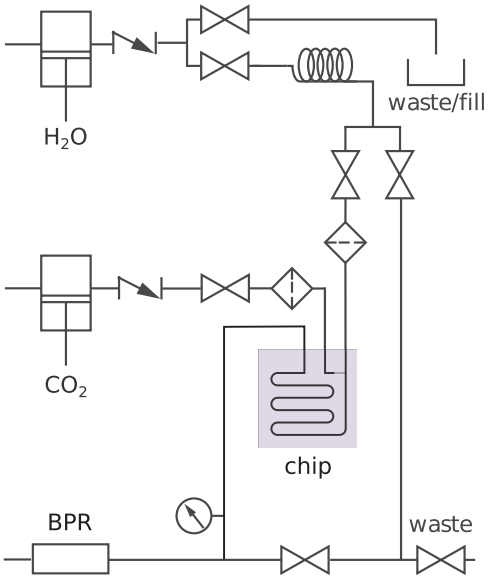

Fig. 1. Schematic drawing of the fluid system and chip. The two pumps (H_2O, CO_2), valves, filters, sample loop, pressure sensor and backpressure regulator (BPR) are shown.

the fluids connect to the chip, 2 µm pore filters (A-355, IDEX) were installed. The pressure was regulated using a back-pressure regulator (26-1700, Tescom) and a pressure sensor (PA-11, Keller), both mounted downstream after the chip. The temperature on the chip was monitored using a 4-wire Pt100 temperature sensor mounted on the chip with thermal paste. The pressure and temperature data were recorded using Matlab (R2017, Mathworks) with two data acquisition units (2001, Keithley and 34970, Agilent).

The chip (12 × 12 × 2.2 mm) was made from borosilicate glass and a full description of the fabrication methods and the fluid inlet assembly can be found elsewhere [26]. All channels had a semi-circular cross section. The CO_2 is brought in contact with the water in the T-junction near the inlet, creating a segmented flow. The meander consisted of semi-circular curves connected to 6 straight channel sections and had a channel depth of 120 µm, a top width of 300 µm and, a total length of 53.7 mm. The CO_2 inlet of the T-junction had a depth of 8 µm and a width of 76 µm.

The chip was mounted in a fixture and placed in a custom-made optical setup. Imaging was done using a high-speed camera (Miro 310, Phantom Vision) mounted on a stereoscope (Nikon, SMZ800) above the fixture. The monochromic light needed for high-speed imaging was provided using a LED array (CXA2520, Cree) and a 590 nm ± 2 nm bandpass filter (FB590, Thorlabs). The LED array was larger than the chip. A homogenous intensity was delivered over the monitored area using a light diffuser. The high-speed camera operated at a frame rate of 1200 fps, resulting in a temporal resolution of 0.83 ms and operated at 12-bit gray scale resolution. To verify that light of the correct wavelength passed the chip, a spectrum was recorded using a fiber coupled spectrometer (CCS200, Thorlabs).

In the first evaluations, a slightly different setup was used to study the local pH-effects and fluid behavior at the initial contact point where CO_2 and the aqueous phase meet and the segmented flow is created. This setup included a similar chip, having a T-junction of the same size as its meander channel. LED light at 430 nm was applied.

2.3. Measurements

Liquid CO_2 segments were injected from the T-junction in the microfluidic chips into the aqueous sample solutions, containing the additive salts and the pH indicator BPB, at a continuous flow while having a back pressure of 80 ± 0.1 bar, a temperature of 24 ± 0.1 °C and a flow rate of 40 µL/min. Pressure and temperature conditions were kept constant during all measurements. Using the response processing described below, by tracking the position of the liquid segments over time using the different video frames, the pH change could be followed as a function of time from the moment when the two phases initially contacted each other at the T-junction. At that location, *i.e.* the contact point in Fig. 2, the interaction time is defined as 0. The description of the calibration method and theory is found in the supplementary information (SI), Appendix A.

A theoretical model was used to enable a comparison to the measured pH at equilibrium with theoretical values, giving a prediction of the pH at equilibrium. The description of this model is found in the SI, Appendix B. To interpret the development of pH equilibrium, a description of the applicable kinetics is used and can be found in the SI, Appendix C. Using this, when the fluid interactions in the chip resulted in the pH reaching a constant level, *i.e.* steady state conditions, a measured pH_{eq} could be determined together with the fitting parameters b and k_{app}, giving an acidification rate constant, k.

2.4. Response processing

From high-speed video and blank images, imaging corresponding to the absorbance at 590 nm was created. Image processing techniques were used to translate the imaging into quantitative data, giving the absorbance response of the aqueous phase along the channel of the chip. With the use of the calibration solutions and by measuring the velocity of the CO_2 segmented flow, the pH can be correlated to the absorbance and length can be translated to time, producing a measurement of pH as a function of time.

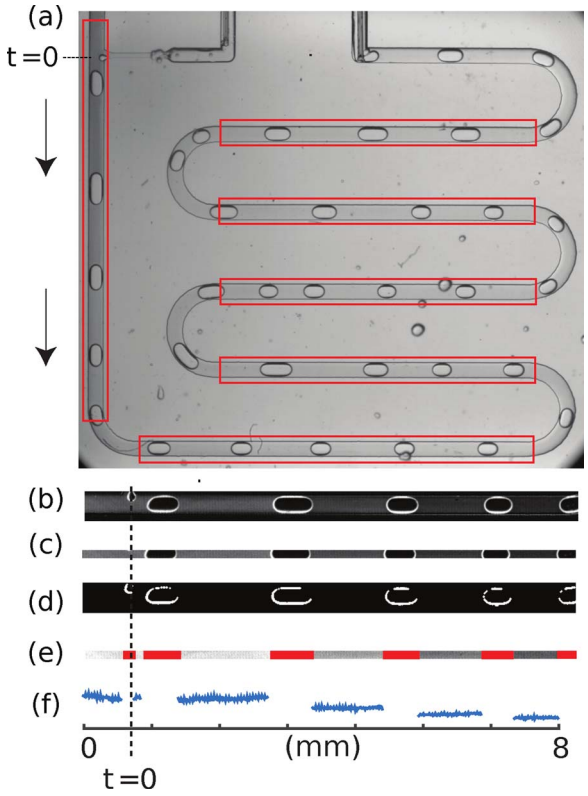

Fig. 2. A description of the image processing procedure from the raw data frames (a), showing the 6 processing regions marked in red rectangles. The absorbance image of the vertical path is shown in (b), followed by the 10 pixels wide, centered, measurement region (c). (d) shows the binary image used to filter CO_2 segments. (e) shows a filtered and contrast adjusted version of (c) where the red regions shows excluded pixels, followed by the corresponding absorbance (f). The location of the contact point of zero interaction time, $t = 0$, is shown in (a) (dashed line) together with the flow direction of the first part of the meander, indicated by two arrows. (For interpretation of the references to colour in this figure legend, the reader is referred to the web version of this article.)

The image processing steps were, in the following order: alignment, pixel-wise calculations, measurement region definition, filtering, averaging and calibration. All image processing were done in Matlab and a description of the imaging processing is shown in Fig. 2. For each measurement, sampling for 0.25 s produced 300 frames into a high-speed video. Each frame of the video was then aligned with a blank image and a set of calibration images, resulting in each pixel containing a data set of the measured intensity for either the blank, the calibrations, or the sample measurements. Within these data sets, the absorbance, A, could be calculated as the following,

$$A = -\log\frac{I_s}{I_b}, \tag{1}$$

with I_s and I_b being the sample and blank intensity. Using a reference point calculated from features in the images belonging to the chip layout, processing regions were defined, marked as red rectangles in Fig. 2. Inside these regions, the channel edges were detected by computing the median absorbance of pixels in the direction along the channel, forming a curve across the channel. The local maximums of the derivate of this curve were used as references to the channel edges, and new 10 pixels wide, centered, measurement regions containing only pixels in the channels were defined. To identify the position of the CO_2 segments, intensity thresholding and morphological operations

over the processing regions were used to produce binary images having a contrast with high correlation to the CO_2 segments. By using these binary images as filters over the measurement regions, absorbance response corresponding to the CO_2 segments was excluded. The remaining valid pixels were first averaged perpendicular to the channel direction, producing about 4300 measurement points as a function of channel length. As both the dimensions of the chip and pixel positions are well defined, each measurement region was stitched together, taking care to position the regions in their correct length position along the channel. The calibration is carried out by measuring images of the 7 calibration solutions flowing in the chip without CO_2. To compensate for the differences in light intensity over the channel, separate calibration curves were produced for each of the cross-sectional channel measurement points, resulting in about 4300 unique regression curves. To filter the response from irregularities, calibration curves having an r^2 of less than 0.99 were excluded. These irregularities were primarily defects blocking the optical path such as dust fibers and etch defects. For the sample solutions, the flow velocity was determined by following the position and time of CO_2 segments in the high-speed video. Using the dimensions of the chip, the flow velocity could be translated into interaction time.

3. Results

3.1. Dynamic interaction conditions

When dense CO_2 and an aqueous solution contact each other, Fig. 3a, a localized region in front of the CO_2 segment of lower pH is formed, visible as a darker region with variations perpendicular to the flow direction. Variation in the absorbance before and after each CO_2 segment could also be seen, Fig. 3b, showing that the pH in the aqueous phase was lower in front of the segments. As the fluids continue further in the meander, approximatively 130 ms, this difference becomes less pronounced, and the aqueous phase becomes homogenous. Thus, for a given fixed point early in the meander, pH of the aqueous flow oscillates between a higher and a lower pH. Given this knowledge, the quantitative measurements of pH change, were performed by sampling the absorbance response for several frames. This allowed for an averaged measurement of the pH change along the channel.

3.2. Quantitative response of pH change

The absorbance response in the channel was in the range of 0.017–0.160 and less than 1% of the calibration curves had a regression coefficient lower than 0.99. A typical calibration curve for a measurement point together with a histogram of regression coefficients can be found in the SI, Appendix A.

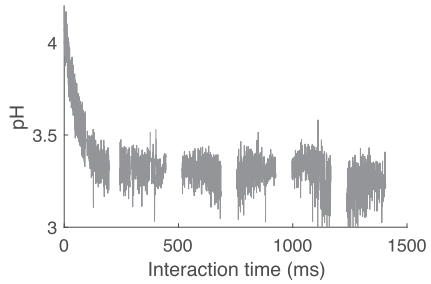

Fig. 4. Interaction time of the aqueous solution containing 2 mM BPB when contacting CO_2. P = 80 ± 0.1 bar T = 24 ± 0.1 °C.

Before contacting the CO_2, the pH of the $NH_4CH_3CO_2$ and NH_4HCO_2 solutions was approximately 7.0. The change of pH with time for an aqueous solution containing only the indicator is shown in Fig. 4. Over the length of the channel, an initial rapid decrease of the pH was followed by a slow approach to a constant level. The segment flow velocities were between 26–47 mm/s, resulting in residence times long enough to reach a stable pH in the chip. The measured pH_{eq} was 3.3 ± 0.2, well in line with the predicted pH_{eq} of 3.1.

The measured pH_{eq} for solutions containing $NH_4CH_3CO_2$ and NH_4HCO_2 is shown in Fig. 5a and b, respectively. In general, both $NH_4CH_3CO_2$ and NH_4HCO_2 produced solutions of a pH higher than 4 when 20 mM of salt is added. Equilibrium was reached in less than 1 s.

The measured pH_{eq}, Fig. 6a, was compared to the prediction using the model presented in the SI, Appendix B. The acidification rate constant k for each concentration is shown in Fig. 6b. When no additive salt was used, k was 2.6 ms^{-1}. For the solutions containing $NH_4CH_3CO_2$ and NH_4HCO_2, the mean of k was 0.30 ms^{-1} and 0.54 ms^{-1}, respectively.

4. Discussion

Using this method, we have been able to visualize the change in pH as dense CO_2 and aqueous solutions mix, giving both temporal and spatial information. At the contact point where the fluids meet, the acidification was dynamic and local lower pH regions were seen in front of the CO_2 segments, Fig. 3. Sampling for several frames and by looking at longer time frames showed the time-averaged pH change along the channel, Fig. 4. This information complements the information of the dynamic behaviour, giving the rates and general timescales required to macroscopically change the pH of the aqueous phase.

The fluid reached steady state conditions, Fig. 4, before exiting the

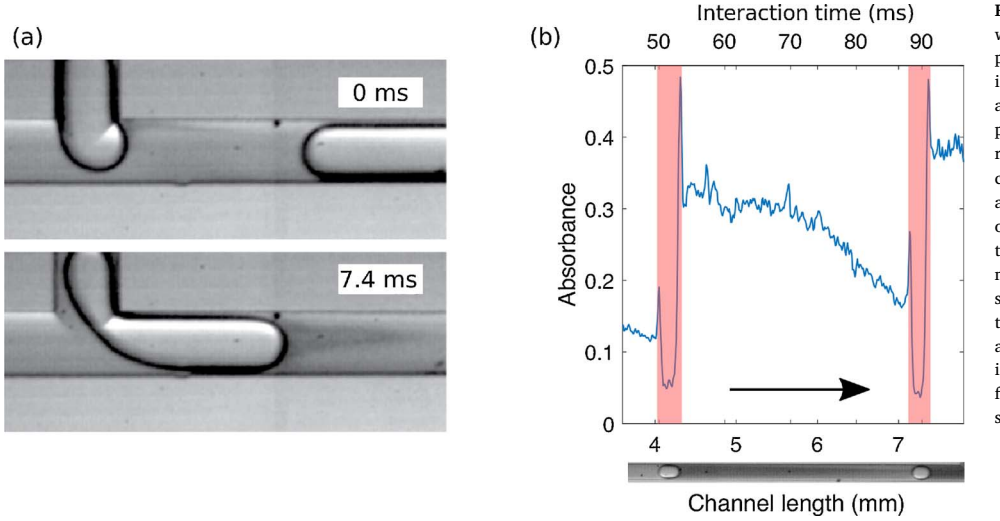

Fig. 3. Interaction effects as CO_2 segments and the water solution contacts each other at the contact point. In (a) CO_2 enters from the top of the image into the T-junction of the chip, flowing to the right at a velocity of 81 mm/s. After 7.4 ms, the segment has progressed further and a triangular shaped localized region of darker intensity and higher absorbance, corresponding to a drop of the pH, has formed around the segments front. In (b) the absorbance for one image frame at 430 nm along the channel close to the contact point is seen, showing two CO_2 segments (marked red) flowing at 81 mm/s with a resulting pH gradient of the aqueous phase in-between the two segments. The flow direction is marked with an arrow. $P = 80 \pm 0.1$ bar $T = 24 \pm 0.1$ °C. (For interpretation of the references to colour in this figure legend, the reader is referred to the web version of this article.)

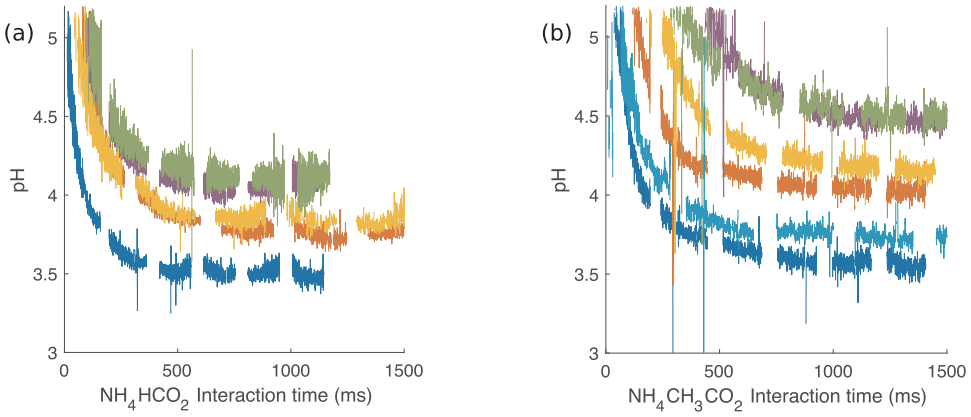

Fig. 5. pH response as a function of interaction time. Each line represents a sample solution of either NH_4HCO_2 (left) and $NH_4CH_3CO_2$ (right), having the concentrations 2 (blue), 5 (cyan), 7 (red), 10 (yellow), 20 (purple) or 30 mM (green). $P = 80 \pm 0.1$ bar $T = 24 \pm 0.1$ °C. (For interpretation of the references to colour in this figure legend, the reader is referred to the web version of this article.)

last measurement region in the chip and the setup allowed for a measurement of pH_{eq}. The measured pH_{eq} correlated well with the predictions made of pH_{eq}, suggesting that the steady state conditions were close to equilibrium. However, as seen in the residuals plot, Fig. 7, there was a small bias and the measured pH values where 0.062 pH units higher compared to the predicted values. The precision of these residuals was 0.086 pH units. Improvements to the optical setup would allow for an increased resolution over the channels and less noise. This would likely also increase the precision. The ionic strength in the aqueous phase increased from 4 to 40 mM as more additive salts were added. This was mainly due to the additions of the ammonium ions and the increasing proportion of bicarbonate ions at higher pH values. As the ionic strength increase, the buffer system becomes more non-ideal. This change the activity and can introduce deviations for the higher ion strengths. Using high-speed multicolour imaging, the concentration of both the deprotonated and protonated species could be measured. It would make it possible to relate the signal response with a pH which is compensated for the ionic strength, *e.g.* by utilizing an absorbance ratio method or chemical regression modelling [27]. Further, this would allow for several indicators to be used, giving a larger measurement range with increased sensitivity.

Fig. 6a provides a measurement of how the additive salts affect the pH in the aqueous phase in contact with CO_2. The pH was very sensitive to additions of additive salts at low concentrations, *i.e.* 2–10 mM. At higher salt concentrations, the pH became less sensitive as there was an excess of basic species from the additive salt compared to the protons generated by the hydration of CO_2. $NH_4CH_3CO_2$ showed a stronger effect on changing the pH than NH_4HCO_2, which can be related to the additive salt anions. By the additions of hydrogen ions from the

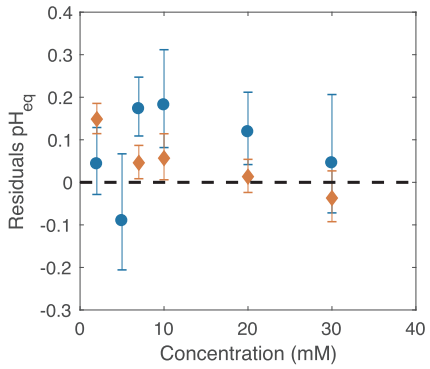

Fig. 7. The residuals, $R = pH_{eq}$(measured) − residuals pH_{eq}(predicted), for NH_4HCO_2 (red diamonds) and $NH_4CH_3CO_2$ (blue circles) are shown together with the prediction line (dashed). (For interpretation of the references to colour in this figure legend, the reader is referred to the web version of this article.)

carbonic acid, the anions are increasingly protonated and the respective conjugate acids, *e.g.* acetic acid and formic acid, are formed. Acetic acid is a weaker acid than formic acid, their respective pKa values being 4.76 and 3.77. The lower degree of dissociation of acetic acid allows for more associated hydrogen ions, resulting in a higher pH. Over the explored pH region, the buffer capacity of the aqueous phase, in contact with CO_2, increases both with the pH and the concentration of additive salt. This is due to the fact that the buffer capacity is affected both by the additive acids and by the carbonic acid. The buffer capacity, β, is described in SI, equation (B.7). Resulting from only the carbonic acid

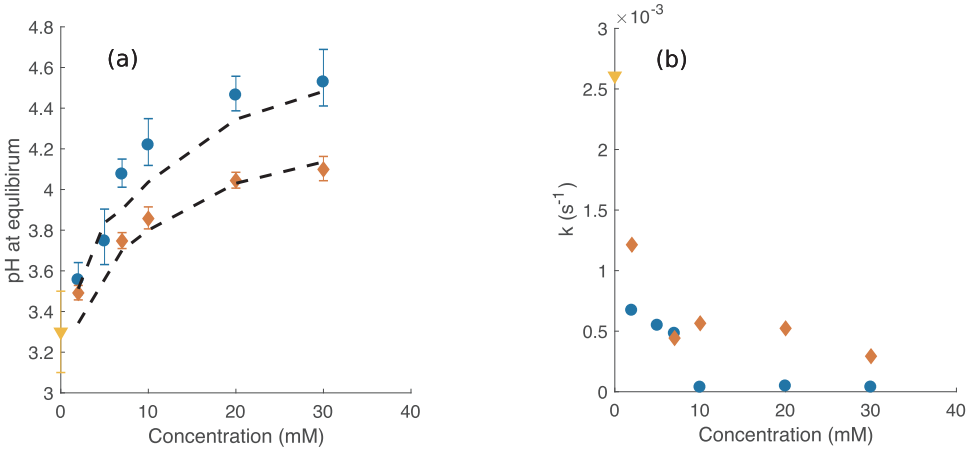

Fig. 6. The measured pH_{eq} is shown in (a) for NH_4HCO_2 (red diamonds), $NH_4CH_3CO_2$ (blue circles) and a solution containing no additive salt (yellow triangle). The calculated prediction of the pH_{eq} is also shown (dashed lines). In (b), the respective rate constants of the acidification are shown for the different solutions ($k = k_{app}b/[CO_2]_{aq}$, $[CO_{2(aq)}] = 1.42$ mol/kg). For all experiments, $P = 80 \pm 0.1$ bar, $T = 24 \pm 0.1$ °C. (For interpretation of the references to colour in this figure legend, the reader is referred to the web version of this article.)

and bicarbonate ions, β is estimated to change from 4 to 46 mM/pH over the pH range 3.3–4.5. At the resultant pH reached by an addition of either 30 mM NH_4HCO_2 or NH_4CH_3CO, *i.e.* 4.1 and 4.5, respectively, β is increased by approximatively 15–18 mM/pH. Thus, 30 mM of added NH_4HCO_2 gives a 78% increase to the buffer capacity, having a clear positive effect on the pH stability. Adding the same amount of $NH_4CH_3CO_2$ gives a smaller increase, 33%. Compared to what is considered a buffer in most applications, β in this study is very low.

The kinetic information of Fig. 4 shows the implications of the high-pressure conditions, where acidification to equilibrium occurred in a few 100 ms. This represents a very different situation from upscaled laboratory experiments at ambient pressures, where the hydration of CO_2 limits the acidification to time scales in the order of 10 s [28]. The solubility of CO_2 in H_2O at 80 bar and 24 °C, *i.e.* 1.42 mol/kg, is in the order of 10^5 times higher than at ambient conditions. Several authors have investigated the rate constant for the limiting hydration reaction, k_{CO_2}, being $37{\cdot}10^{-3}\,s^{-1}$ [29,30] at 25 °C under acidic conditions. k_{CO_2} have further been shown to increase with temperature, ranging from $4.5{\cdot}10^{-3}$ to $236{\cdot}10^{-3}\,s^{-1}$ over the temperature range 6.6–42.8 °C [30]. Our measured rates of acidification, *k*, Fig. 6b, are all lower than k_{CO_2} over this temperature range and suggest even slower reaction rates. While the CO_2 flow can under some conditions produce local cooling effects in the channels [31], the flow conditions used in this study should only have a minor effect on the fluid temperature. More likely, mass transport limits the acidification in the channel. The qualitative response, Fig. 3, also agrees with this observation since localized regions of lower acidity can be identified in the proximity of the CO_2 segments. The acidification was strongly amplified by the fact that relatively low concentrations of CO_2 in the aqueous phase resulted in large changes in pH. For an aqueous solution containing only the indicator, only a fraction, < 0.06 mol%, of CO_2 hydrolyses and dissociates into HCO_3^- and H^+. At timescales in the range of hundreds of ms, the acidification changes are fast but of interest for ultra-fast SFC analysis [3], reaching for retention times less than 1 min. Here, the demand for short timescales is higher as the mobile phase stability after injection needs to develop fast. Methods to determine the time scale of the acidification as well as to being able to study the dynamics involved when different phases meet are therefore important, especially for the miniaturization of chromatographic systems. The timescales limit the miniaturization of SFC-systems, as requirements are put on residence times. As timescales measured in this paper are found to still be mass transport controlled, better mixing can give even shorter timescales. Commercial SFC instruments have dedicated mixing units, *e.g.* metal bead convection-based mixers, and efficient mixing can be achieved in microfluidics [32].

Studies of the influence of $NH_4CH_3CO_2$ concentration on the separation performance of amines in SFC have shown how concentrations, from 0.3 to 15 mM of $NH_4CH_3CO_2$, lowered retention and improves peak shape, reaching a minimal peak asymmetry at 15 mM [20]. A methanol-scCO_2 mobile phase was used together with a 2-ethyl pyridine stationary phase. The paper points out that the acidity of the methanol-scCO_2 mobile phase affects the retention mechanisms, being affected by the partial protonation of the nitrogen atom belonging to the pyridine groups. As shown from the data in Fig. 6, such additions of $NH_4CH_3CO_2$ increase the pH to a more stable region with a higher buffer capacity. Having methods to study both the dynamics and the equilibriums of systems containing water, CO_2 as well as mobile phase additives is of importance, especially when there are needs to also miniaturize the system.

For fast screening and precise studies of interactions between multiphase flows, there are clear advantages of using microchips [33]. As the timescale to reach steady-state conditions and data collection was here only about 0.25 s, the method described in this paper would be suitable for future screening studies of the *P, T* space. The major limitation is reaching a stable pressure and temperature in the microfluidic chip. However, in microfluidics, both the small mass of chips and the high surface to volume ratio generally results in good thermal transfer and quick changes of setpoint conditions. To further control the temperature, it is possible to advance the method with integrated temperature sensors [31]. The overall measurement time, dependent on when stable condition of the flow rate and pressure is reached, was about 100 s. The microchip can handle pressures up to approximately 120 bar and using the high-speed camera, flow rates up to 150 mm/s are possible to evaluate. An increase in temperature will reduce the lifetime of the microfluidic chip if high pressures are used as described in [26]. However, if pressures above approximately 120 bar is to be evaluated, there will be a need to reduce the channels dimensions to achieve a higher durability of the chip.

The high-speed camera was necessary to visualize the dynamics when the phases meet and interact, and it allowed for a clear signal response of the general acidification in the aqueous phase. Detector systems with lower time resolution would not have been able to distinguish if the signal is generated from the CO_2 or aqueous phase segments. Alternatively, other approaches such as separating the segments after they have interacted could be explored to study the changes of pH in the water phase, but then, the opportunity to study the dynamic changes would have been lost.

5. Conclusion

A system has been developed consisting of a high-pressure chip for segmented flows in combination with a high-speed camera to study rapid dynamic events. To demonstrate its capabilities, a method to allow for fast screening and visualization of pH conditions in high-pressure fluids has been presented. At 80 ± 0.1 bar and 24 ± 0.1 °C, 30 mM of either ammonium acetate or ammonium formate resulted in significant changes to the pH of an aqueous phase as dense CO_2 contacts, with a resulting pH of 4.5 and 4.1, respectively. In the microfluidic chip, acidification occurred at timescales less than 1 s. As the two phases contacted each other, a local pH drop can be identified in front of CO_2 segments. Given the measured rate constants of the acidification, the system is found to be mass transport controlled.

Conflict of interest

The authors declare no competing financial interest.

Acknowledgement

The funding for the laboratory facilities by the Knut and Alice Wallenberg Foundation is acknowledged.

Appendix A–C.

Supplementary data associated with this article can be found, in the online version, at https://doi.org/10.1016/j.supflu.2018.02.012.

References

[1] D. Mark, S. Haeberle, G. Roth, F. Stettenz, R. Zengerle, Microfluidic lab-on-a-chip platforms: requirements, characteristics and applications, Chem. Soc. Rev. 39 (2010) 1153–1182.
[2] B. Pinho, S. Girardon, F. Bazer-Bachi, G. Bergeot, S. Marre, C.A. Aymonier, A microfluidic approach for investigating multicomponent system thermodynamics at high pressures and temperatures, Lab Chip 14 (2014) 3843–3849.
[3] A. Grand-Guillaume Perrenoud, J. Veuthey, D. Guillarme, Comparison of ultra-high performance supercritical fluid chromatography and ultra-high performance liquid chromatography for the analysis of pharmaceutical compounds, J. Chromatogr. A 1266 (2012) 158–167.
[4] J.P. Grinias, R.T. Kennedy, Advances in and prospects of microchip liquid chromatography, Trends Anal. Chem. 81 (2016) 110–117.
[5] M. Saito, History of supercritical fluid chromatography: instrumental development, J. Biosci. Bioeng. 115 (2013) 590–599.
[6] L.T. Taylor, Packed column supercritical fluid chromatography of hydrophilic analytes via water-rich modifiers, J. Chromatogr. A 1250 (2012) 196–204.

[7] F.O. Geiser, S.G. Yocklovich, S.M. Lurcott, J.W. Guthrie, E.J. Levy, Water as a stationary phase modifier in packed-column supercritical fluid chromatography: I. Separation of free fatty acids, J. Chromatogr. A 459 (1988) 173–181.
[8] A. Salvador, B. Herbreteau, M. Lafosse, M. Dreux, Subcritical fluid chromatography of monosaccharides and polyols using silica and trimethylsilyl columns, J. Chromatogr. A 785 (1997) 195–204.
[9] H. Yuan, S.V. Olesik, Comparison of reversed-phase HPLC separation using carbon dioxide and fluoroform for enhanced-fluidity liquid mobile phases, Anal. Chem. 70 (1998) 1595–1603.
[10] J.W. Treadway, G.S. Philibert, S.V. Olesik, Enhanced fluidity liquid chromatography for hydrophilic interaction separation of nucleosides, J. Chromatogr. A 1218 (2011) 5897–5902.
[11] M.C. Beilke, M.J. Beres, S.V. Olesik, Gradient enhanced-fluidity liquid hydrophilic interaction chromatography of ribonucleic acid nucleosides and nucleotides: a green technique, J. Chromatogr. A 1436 (2016) 84–90.
[12] R.F. Venn, Principles and Practice of Bioanalysis, Second ed., CRC Press, Boca Raton, 2008, p. 71.
[13] U.D. Neue, C.H. Phoebe, K. Tran, Y. Cheng, Z. Lu, Dependence of reversed-phase retention of ionizable analytes on pH, concentration of organic solvent and silanol activity, J. Chromatogr. A 925 (2001) 49–67.
[14] C. West, J. Melin, H. Ansouri, M.M. Metogo, Unravelling the effects of mobile phase additives in supercritical fluid chromatography. Part I: polarity and acidity of the mobile phase, J. Chromatogr. A 1492 (2017) 136–143.
[15] D. Wen, S.V. Olesik, Characterization of pH in liquid mixtures of methanol/H2O/CO2, Anal. Chem. 72 (2000) 475–480.
[16] S. Wang, S. Elshani, C.M. Wai, Selective extraction of mercury with ionizable crown ethers in supercritical carbon dioxide, Anal. Chem. 67 (1995) 919–923.
[17] K.L. Toews, R.M. Shroll, C.M. Wai, N.G. Smart, pH-defining equilibrium between water and supercritical CO2. Influence on SFE of organics and metal chelates, Anal. Chem. 67 (1995) 4040–4043.
[18] D.P. Poe, D. Veit, M. Ranger, K. Kaczmarski, A. Tarafder, G. Guiochon, Pressure, temperature and density drops along supercritical fluid chromatography columns. I. Experimental results for neat carbon dioxide and columns packed with 3- and 5-micron particles, J. Chromatogr. A 1250 (2012) 105–114.
[19] Brian G. Cox, Acids and Bases Solvent Effects on Acid-Base Strength, Oxford Scholarship Online, 2013.
[20] A. Cazenave-Gassiot, R. Boughtflower, J. Caldwell, L. Hitzel, C. Holyoak, S. Lane, P. Oakley, F. Pullen, S. Richardson, G.J. Langley, Effect of increasing concentration of ammonium acetate as an additive in supercritical fluid chromatography using CO2–methanol mobile phase, J. Chromatogr. A 1216 (2009) 6441–6450.
[21] L. Nováková, A. Grand-Guillaume Perrenoud, R. Nicoli, M. Saugy, J. Veuthey, D. Guillarme, Ultra high performance supercritical fluid chromatography coupled with tandem mass spectrometry for screening of doping agents. I: investigation of mobile phase and MS conditions, Anal. Chim. Acta 853 (2015) 637–646.
[22] H.R. Hobbs, N.R. Thomas, Biocatalysis in supercritical fluids, in fluorous solvents, and under solvent-free conditions, Chem. Rev. 107 (2007) 2786–2820.
[23] M.T. Combs, M. Ashraf-Khorassani, L.T. Taylor, pH effects on the direct supercritical fluid extraction of phenols from aqueous matrices, J. Supercrit. Fluids 9 (1996) 122–127.
[24] J.D. Holmes, K.J. Ziegler, M. Audriani, C.T. Lee, P.A. Bhargava, D.C. Steytler, K.P. Johnston, Buffering the aqueous phase pH in water-in-CO2 microemulsions, J. Phys. Chem. B 103 (1999) 5703–5711.
[25] C. Roosen, M. Ansorge-Schumacher, T. Mang, W. Leitner, L. Greiner, Gaining pH-control in water/carbon dioxide biphasic systems, Green Chem. 9 (2007) 455–458.
[26] M. Andersson, K. Hjort, L. Klintberg, Fracture strength of glass chips for high-pressure microfluidics, J. Micromech. Microeng. 26 (2016) 095009.
[27] H. Shao, C.J. Thompson, O. Qafoku, K.J. Cantrell, In situ spectrophotometric determination of pH under geologic CO2 sequestration conditions: method development and application, Environ. Sci. Technol. 47 (2013) 63–70.
[28] A. Persat, R.D. Chambers, J.G. Santiago, Basic principles of electrolyte chemistry for microfluidic electrokinetics. Part I: acid–base equilibria and pH buffers, Lab Chip 9 (2009) 2437–2453.
[29] B.H. Gibbons, J.T. Edsall, Rate of hydration of carbon dioxide and dehydration of carbonic acid at 25°C, J. Biol. Chem. 238 (1963) 3502–3507.
[30] X. Wang, W. Conway, R. Burns, N. McCann, M. Maeder, Comprehensive study of the hydration and dehydration reactions of carbon dioxide in aqueous solution, J. Phys. Chem. A 114 (4) (2010) 1734–1740.
[31] M. Andersson, J. Ek, L. Hedman, F. Johansson, V. Sehlstedt, J. Stocklassa, P. Snögren, V. Pettersson, J. Larsson, O. Vizuete, K. Hjort, L. Klintberg, Thin film metal sensors in fusion bonded glass chips for high-pressure microfluidics, J. Micromech. Microeng. 27 (2017) 015018.
[32] N. Nguyen, Z. Wu, Micromixers—a review, J. Micromech. Microeng. 15 (2005) R1.
[33] S. Marre, Y. Roig, C. Aymonier, Supercritical microfluidics: oppertunities in flow through chemistry and materials science, J. Supercrit. Fluids 66 (2012) 251–264.